



Sub-arcsecond (Sub)millimeter Imaging of the Massive Protocluster G358.93–0.03: Discovery of 14 New Methanol Maser Lines Associated with a Hot Core

C. L. Brogan¹ , T. R. Hunter¹ , A. P. M. Towner^{1,2,27} , B. A. McGuire^{1,3,28} , G. C. MacLeod^{4,5}, M. A. Gurwell³ , C. J. Cyganowski⁶ , J. Brand^{7,8}, R. A. Burns^{9,10} , A. Caratti o Garatti¹¹ , X. Chen¹², J. O. Chibueze^{13,14} , N. Hirano¹⁵, T. Hirota^{9,16} , K.-T. Kim¹⁰ , B. H. Kramer^{17,18}, H. Linz¹⁹, K. M. Menten¹⁷, A. Remijan¹ , A. Sanna¹⁷, A. M. Sobolev²⁰, T. K. Sridharan³, B. Stecklum²¹, K. Sugiyama²² , G. Surcis²³, J. Van der Walt²⁴, A. E. Volvach^{25,26}, and L. N. Volvach²⁵

¹National Radio Astronomy Observatory, 520 Edgemont Road, Charlottesville, VA 22903, USA; cbrogan@nrao.edu

²Department of Astronomy, University of Virginia, P.O. Box 3818, USA

³Center for Astrophysics | Harvard & Smithsonian, Cambridge, MA 02138, USA

⁴Hartebeesthoek Radio Astronomy Observatory, P.O. Box 443, Krugersdorp 1740, South Africa

⁵The University of Western Ontario, 1151 Richmond Street, London, ON N6A 3K7, Canada

⁶SUPA, School of Physics and Astronomy, University of St. Andrews, North Haugh, St. Andrews KY16 9SS, UK

⁷INAF-Istituto di Radioastronomia, via P. Gobetti 101, I-40129 Bologna, Italy

⁸Italian ALMA Regional Centre, via P. Gobetti 101, I-40129 Bologna, Italy

⁹Mizusawa VLBI Observatory, National Astronomical Observatory of Japan, Osawa 2-21-1, Mitaka, Tokyo 181-8588, Japan

¹⁰Korea Astronomy and Space Science Institute, 776 Daedeokdae-ro, Yuseong-gu, Daejeon 34055, Republic of Korea

¹¹Dublin Institute for Advanced Studies, 31 Fitzwilliam Place, D02 XF86, Dublin, Ireland

¹²Center for Astrophysics, GuangZhou University, Guangzhou 510006, People's Republic of China

¹³Space Research Unit, Physics Department, North-West University, Potchefstroom, 2520, South Africa

¹⁴Department of Physics and Astronomy, University of Nigeria, Carver Building, 1 University Road, Nsukka, 410001, Nigeria

¹⁵Institute of Astronomy and Astrophysics, Academia Sinica, 11F of Astronomy-Mathematics Building, AS/NTU, No.1, Sec. 4, Roosevelt Rd, Taipei 10617, Taiwan, R.O.C.

¹⁶Department of Astronomical Sciences, SOKENDAI (The Graduate University for Advanced Studies), Osawa 2-21-1, Mitaka-shi, Tokyo 181-8588, Japan

¹⁷Max-Planck-Institut für Radioastronomie, Auf dem Hügel 69, D-53121 Bonn, Germany

¹⁸National Astronomical Research Institute of Thailand, 260 Moo 4, T. Donkaew, Amphur Maerim, Chiang Mai, 50180, Thailand

¹⁹Max Planck Institute for Astronomy, Königstuhl 17, D-69117 Heidelberg, Germany

²⁰Ural Federal University, 19 Mira street, 620002 Ekaterinburg, Russia

²¹Thüringer Landessternwarte, Sternwarte 5, D-07778 Tautenburg, Germany

²²National Astronomical Observatory of Japan, Osawa 2-21-1, Mitaka-shi, Tokyo 181-8588, Japan

²³INAF-Osservatorio Astronomico di Cagliari, Via della Scienza 5, I-09047, Selargius, Italy

²⁴Centre for Space Research, North-West University, Potchefstroom, South Africa

²⁵Radio Astronomy Laboratory of Crimean Astrophysical Observatory, Katsively, RT-22, Crimea[†]

²⁶Institute of Applied Astronomy, Russian Academy of Sciences, St. Petersburg, Russia

Received 2019 May 31; revised 2019 June 30; accepted 2019 July 4; published 2019 August 20

Abstract

We present (sub)millimeter imaging at 0".5 resolution of the massive star-forming region G358.93–0.03 acquired in multiple epochs at 2 and 3 months following the recent flaring of its 6.7 GHz CH₃OH maser emission. Using the Submillimeter Array and Atacama Large Millimeter/submillimeter Array, we have discovered 14 new Class II CH₃OH maser lines ranging in frequency from 199 to 361 GHz, which originate mostly from $v_t = 1$ torsionally excited transitions and include one $v_t = 2$ transition. The latter detection provides the first observational evidence that Class II maser pumping involves levels in the $v_t = 2$ state. The masers are associated with the brightest continuum source (MM1), which hosts a line-rich hot core. The masers present a consistent curvilinear spatial velocity pattern that wraps around MM1, suggestive of a coherent physical structure 1200 au in extent. In contrast, the thermal lines exhibit a linear pattern that crosses MM1 but at progressive position angles that appear to be a function of either increasing temperature or decreasing optical depth. The maser spectral profiles evolved significantly over one month, and the intensities dropped by factors of 3.0–7.2, with the $v_t = 2$ line showing the largest change. A small area of maser emission from only the highest excitation lines closest to MM1 has disappeared. There are seven additional dust continuum sources in the protocluster, including another hot core (MM3). We do not find evidence for a significant change in (sub)millimeter continuum emission from any of the sources during the one month interval, and the total protocluster emission remains comparable to prior single-dish measurements.

Key words: ISM: individual objects (G358.93–0.03) – masers – stars: formation – stars: protostars

1. Introduction

The recent discoveries of powerful accretion outbursts in two high-mass protostars—NGC 6334I-MM1 (Hunter et al. 2017, 2018) and S255IR-NIRS3 (Caratti o Garatti et al. 2017; Liu et al. 2018)—have provided crucial insights on the role of episodic accretion in massive star formation (Brogan et al. 2018; Cesaroni et al. 2018). A recent study of Orion

²⁷ A.P.M.T. is a Grote Reber Doctoral Fellow at NRAO.

²⁸ B.A.M. is a Hubble Fellow of the National Radio Astronomy Observatory.

While the AAS journals adhere to and respect UN resolutions regarding the designations of territories (available at <http://www.un.org/press/en>), it is our policy to use the affiliations provided by our authors on published articles.

suggests that episodic accretion accounts for $\gtrsim 25\%$ of a star’s mass (Fischer et al. 2019), suggesting it is an important process in star formation. Both aforementioned outbursts were heralded by 6.7 GHz CH₃OH maser flares (Fujisawa et al. 2015; MacLeod et al. 2018; Szymczak et al. 2018), and subsequent high-resolution studies confirmed that the flares occurred in dense gas surrounding the outbursting protostar (Moscadelli et al. 2017; Hunter et al. 2018), motivating new hydrodynamic simulations of protostellar accretion (Meyer et al. 2019a, 2019b). Because Class II CH₃OH masers are pumped by infrared radiation (Cragg et al. 2005), their apparent association with protostellar luminosity outbursts has a theoretical basis. Thus, identifying and characterizing more events is critical to understanding massive star formation, which has inspired the international maser community to form the M2O group³⁰ to coordinate single-dish monitoring of masers and to perform rapid interferometric follow-up (e.g., Burns et al. 2018). As a result, we are now better positioned to identify new outbursts, and catch them earlier in their evolution.

On 2019 January 14, the 6.7 GHz Class II CH₃OH maser line in the massive star-forming region G358.93–0.03 began flaring, rising in flux by an order of magnitude to 99 Jy after two weeks (Sugiyama et al. 2019). Maser emission in this transition toward this region was previously reported by Caswell et al. (2010, epoch 2006.24) with a peak flux density of 10 Jy at $v_{\text{LSR}} = -15.9 \text{ km s}^{-1}$ and by Rickert et al. (2019, epoch 2015.69; 1.7 Jy at -18.7 km s^{-1}). This region appears as a compact clump in single-dish (sub)millimeter continuum surveys including the 1.1 mm BOLOCAM Galactic Plane Survey (BGPS) (G358.936–00.032, Rosolowsky et al. 2010) and the 0.87 mm ATLASGAL survey (AGAL358.931-00.029, Urquhart et al. 2013). Otherwise, this field has been poorly studied, with no prior (sub)millimeter interferometric observations.

Because the 6.7 GHz CH₃OH maser flare in G358.93–0.03 may be indicative of a massive protostellar outburst event, the M2O group has pursued multi-wavelength follow-up with telescopes worldwide, leading to the unprecedented discovery of several never-before-seen Class II CH₃OH maser lines, including some in the torsionally excited ($v_t = 1$) state. The first published results are the centimeter wavelength lines (Breen et al. 2019; Volvach et al. 2019). Light curves of the more common ($v_t = 0$) maser lines from Hartebeesthoek Radio Observatory (MacLeod et al. 2019) show that the emission rose more rapidly than in NGC 6334I-MM1 (8 months, MacLeod et al. 2018) and S255IR-NIRS3 (5 months, Szymczak et al. 2018). While some velocity components have peaked, they persisted longer than the initial rise time, and other velocity components have emerged. Thus, in contrast to the earlier cases, we have caught this flare during its initial rise, and additional follow-up is ongoing (Bayandina et al. 2019, in preparation; R. Burns et al. 2019, in preparation, Chen et al. 2019). In this paper, we report first results from 0.87 to 1.5 mm Submillimeter Array (SMA) and Atacama Large Millimeter/submillimeter Array (ALMA) observations taken $\sim +2$ and $\sim +3$ months after the 6.7 GHz maser flare began.

2. Observations

The observing parameters of our SMA and ALMA data are summarized in Table 1. The SMA data were calibrated in MIR, and the ALMA data were calibrated using the ALMA CASA pipeline. The SMA employed 8 antennas while ALMA employed 43, and the calibrators in each observation are listed in Table 1. For consistency, ALMA flux monitoring data was used to set the absolute flux scale for all the observations.³¹ We estimate that the absolute flux calibration uncertainty is 5% and 10% for the ALMA and SMA data, respectively. All of the data were imaged in CASA 5.4.0-70, and self-calibrated using the strongest maser channel in each respective band. The SMA 290.3 and 306.3 GHz windows did not contain any maser emission and are not discussed further.

The SMA continuum images were made with robust weighting $R = +0.5$ and have beam sizes of $0''.66 \times 0''.46$ ($pa = +4^\circ$) at 210.88 GHz and $1''.1 \times 0''.7$ ($pa = +14^\circ$) at 346 GHz. The ALMA continuum images were made with $R = -0.5, +0.1, \text{ and } +0.1$ for Bands 5, 6, and 7 (1.5, 1.3, and 0.89 mm), respectively, yielding similar angular resolutions that were subsequently convolved to a common beam of $0''.46 \times 0''.42$ ($pa = -30^\circ$) to measure the individual source properties. An $R = +1.0$ Band 7 image was also created to measure the integrated flux density for comparison to single-dish measurements. Small systematic position offsets among the continuum images were removed using the ALMA Band 5 195 GHz image as the reference (see Table 1). The ALMA Band 5 absolute position uncertainty is estimated to be <40 mas.

3. Results

3.1. (Sub)millimeter Continuum and Thermal Line Emission

As shown in Figure 1(a), we resolve G358.93–0.03 into a protocluster of eight (sub)millimeter continuum sources at an angular resolution of $0''.46 \times 0''.42$ at 0.89 mm. These sources have been designated MM1...MM8 in order of decreasing R.A. The morphology is consistent from 0.89 to 1.5 mm and across the SMA and ALMA epochs. The projected linear separations between nearest neighbors are a few thousand to 10,000 au (assuming a distance 6.75 kpc, see below for details), which is typical of other regions of massive star formation (Brogan et al. 2016; Beuther et al. 2018). The integrated flux density of G358.93–0.03 at 0.89 mm from the $R = +1.0$ ALMA image is 1.13 ± 0.03 Jy.

The continuum images from the three ALMA bands, and the SMA 210.88 GHz image, were fit with eight 2D Gaussian components (the resolution of the 346 GHz SMA data is too poor to resolve the majority of sources); the fitted properties are provided in Table 2. After subtracting the model components, two areas of residual emission are consistently present across all the images. The brightest is from diffuse emission between MM1 and MM3, which appears to be a “bridge” connecting the two and not a distinct source; the second is compact and located at the peak position of MM1, suggesting additional unresolved structure not well fit by a single Gaussian. For the ALMA 1.5–0.89 mm images, the “bridge” has peak intensities of 3.4, 7.0, and 23.5 mJy beam⁻¹, while the MM1 residual has peak intensities of 2.4, 5.1, and 18.7 mJy beam⁻¹.

³⁰ See the Maser Monitoring Organization (M2O) website at MaserMonitoring.org.

³¹ ALMA Source Catalog: <https://almascience.eso.org/sc>.

Table 1
Observations Summary

Band(s)	Date	Time on G358 (minute)	PWV ^a (mm)	uv Range ^b (kilo- λ)	Spectral Window Frequencies ^c (GHz)	Calibrators ^d	Position Offset ^e	rms Cont./Line ^f (mJy beam ⁻¹)
SMA								
240/345	2019 Mar 14	187	0.3	24–344	202.0 (A), 218.0 (A) 290.3 (A), 306.3 (A)	J1700-261/J1733-130 (Ga,Fl), J1744-312, 3C279	−0 [′] 144, −0 [′] 012	0.48/120
345/400	2019 Mar 22	134	0.4	18–200	334.0 (A), 342.0 (A) 350.0 (A), 358.0 (A)	J1700-261/J1733-130 (Ga,Fl), 3C279, J1924-292	−0 [′] 075, −0 [′] 088	2.0/300
ALMA								
Band 5	2019 Apr 16	55	0.9	9–494	189.033 (B), 189.523 (B) 199.610 (C), 200.925 (C), 201.765 (D), 202.295 (D)	J1924-292 (Fl), J1744-312 (Ga)	0 [′] 0, 0 [′] 0	0.14/2.8
Band 6	2019 Apr 16	55	0.9	11–590	225.936 (E), 229.629 (F) 240.762 (E), 241.622 (E)	J1924-292 (Fl), J1744-312 (Ga)	+0 [′] 015, +0 [′] 011	0.12/2.5
Band 7	2019 Apr 12	49	0.6	16–725	330.231 (G), 330.858 (G), 331.814 (H), 342.943 (H), 343.660 (G), 344.373 (G)	J1924-292 (Fl), J1744-312 (Ga)	−0 [′] 007, −0 [′] 033	0.35/7.2

Notes.

^a Mean precipitable water vapor at zenith.

^b Range of projected baseline lengths.

^c The bandwidth (MHz), and channel width (kHz) are indicated by the following letter codes: A: 8000, 140; B: 117, 61; C: 234, 122; D: 468, 244; E: 937.5, 244; F: 234, 61; G: 117, 122 ; H: 937.5, 488.

^d Absolute flux and complex gain calibrators are marked with (Fl) and/or (Ga), respectively. All listed calibrators were used for SMA bandpass calibration, while J1924-292 was used for the ALMA observations.

^e The Band 5 ALMA continuum image was used as the reference to remove small position offsets from the other data sets; these offsets were also applied to the line data.

^f Aggregate continuum rms noise and representative noise per 0.21 or 0.12 km s⁻¹channel for SMA and ALMA, respectively.

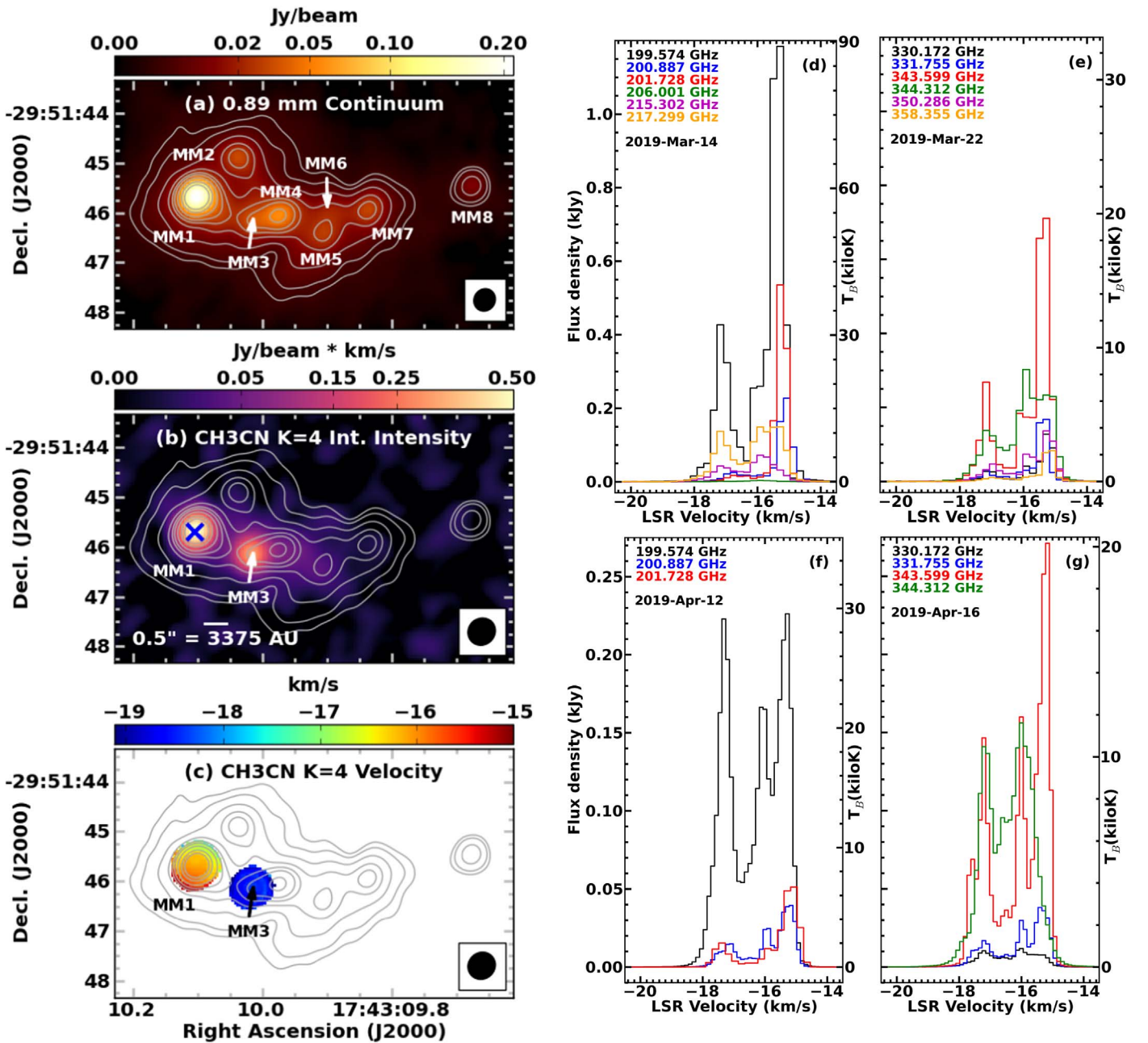


Figure 1. (a) ALMA 0.89 mm (Band 7) continuum image of G358.93–0.03, with an angular resolution $0''.46 \times 0''.42$ (~ 3000 au at 6.75 kpc). The contour levels are $3.5 \text{ mJy beam}^{-1} (1\sigma) \times (8, 12, 24, 48, 72, 96, 144, 240, 336)$; the continuum components are labeled for reference. Integrated intensity (b) and velocity (c) images of the CH₃CN $J = 11_4-10_4$ transition (Band 5 data, beam $0''.55$), with the 0.89 mm contours from (a) overlaid. The location of the (sub)millimeter masers is indicated by the blue \times symbol in (b). (d–g) Spatially integrated maser spectra for (d) SMA, near 200 GHz; (e) SMA, near 340 GHz; (f) ALMA, for three of the same lines as panel (d); and (g) ALMA, for four of the same lines as panel (e). The brightness temperature (T_b) scales (shown in kiloKelvin) are computed with respect to the synthesized beam, not the fitted size.

Figure 1(b) shows the integrated intensity of the CH₃CN $J = 11_4-10_4$ transition ($E_{\text{upper}}/k = 172.5$ K), revealing that G358.93–0.03 harbors two molecular hot cores coincident with MM1 and MM3, with MM1 showing significantly richer spectra. Using hot core tracers, the center velocity of MM1 is $v_{\text{LSR}} = -16.5 \pm 0.3 \text{ km s}^{-1}$ and the FWHM line width is $\Delta V = 3.1 \pm 0.2 \text{ km s}^{-1}$. For MM3, $v_{\text{LSR}} = -18.6 \pm 0.2 \text{ km s}^{-1}$ and $\Delta V = 3.7 \pm 0.2 \text{ km s}^{-1}$. Figure 1(c) demonstrates that hot core tracers like CH₃CN show a roughly north–south velocity gradient across MM1, while MM3 shows little velocity variation at the current angular resolution.

Lacking a maser parallax distance, we use the MM1 v_{LSR} to derive a near kinematic distance of 6.75 kpc (model A5, Reid et al. 2014, see http://bessel.vlbi-astrometry.org/revised_kd_2014). This estimate has considerable uncertainty ($+0.37$, -0.68 kpc reported by the model) due to the proximity of the source to the Galactic center.

The MM1 fitted continuum size ($0''.26 \times 0''.22$, Table 2) is near the lower limit that can be probed with the current resolution data, thus the true source size may well be smaller. Indeed, the methyl cyanide (CH₃CN) $J = 11-10$, $K = 0-6$ emission is well matched to a single excitation temperature model with $T_{\text{ex}} = 172 \pm 3$ K and a background temperature

Table 2
Continuum Source Properties

Source	J2000 Fitted Position ^a		Fitted Size ^b major \times minor, pa (σ_{size} , σ_{pa}) " \times ", ° (" , °)	ALMA Flux Density			Spectral Index Fit	SMA Flux Density (mJy) 210.88 GHz	Percent ^c Diff. Epochs
	R.A.	Decl.		(mJy)					
				195.58 GHz	233.75 GHz	337.26 GHz			
MM1	17:43:10.1014 (0.0005)	−29:51:45.693 (0.002)	0.26 \times 0.22, +80 (0.02, 2)	52.5 (0.3)	96.7 (0.3)	281.8 (0.8)	3.06 (0.13)	70.1 (0.9)	+3.3
MM2	17:43:10.036 (0.001)	−29:51:44.935 (0.005)	0.51 \times 0.41, +67 (0.06, 4)	8.7 (0.4)	18.3 (0.4)	64.4 (1.2)	3.60 (0.15)	11.0 (1.3)	−8.4
MM3	17:43:10.024 (0.002)	−29:51:46.123 (0.02)	0.56 \times 0.32, +50 (0.04, 13)	5.4 (0.4)	10.4 (0.4)	39.9 (1.1)	3.67 (0.17)	7.1 (0.9)	+0.0
MM4	17:43:09.975 (0.001)	−29:51:46.065 (0.009)	0.55 \times 0.29, +82 (0.04, 2)	15.4 (0.4)	26.0 (0.4)	93.5 (1.1)	3.34 (0.13)	20.7 (1.3)	+7.4
MM5	17:43:09.908 (0.001)	−29:51:46.435 (0.005)	0.57 \times 0.42, +137 (0.03, 9)	7.9 (0.4)	13.4 (0.4)	50.6 (1.2)	3.47 (0.16)	10.0 (1.5)	+1.7
MM6	17:43:09.900 (0.008)	−29:51:45.92 (0.07)	<0.4	1.6 (0.2)	3.1 (0.2)	9.9 (0.4)	3.28 (0.22)	2.6 (0.4)	...
MM7	17:43:09.841 (0.001)	−29:51:45.96 (0.05)	0.52 \times 0.35, +122 (0.07, 2)	8.9 (0.4)	14.6 (0.3)	62.5 (1.2)	3.68 (0.15)	11.1 (1.3)	+2.1
MM8	17:43:09.677 (0.001)	−29:51:45.49 (0.05)	<0.2	2.9 (0.3)	4.9 (0.2)	13.3 (0.7)	2.77 (0.21)	3.4 (0.9)	...

Notes.

^a From the 195.58 GHz ALMA Band 5 fits, the 1σ uncertainty includes the dispersion among the ALMA bands.

^b Error-weighted fitted mean deconvolved size from the three ALMA bands; the 1σ uncertainties include the dispersion between bands and fitting uncertainty added in quadrature. An upper limit is given when the deconvolved size could not be measured.

^c Percent difference of the SMA 210.88 GHz flux density (epoch 2019.20) relative to the value predicted at this frequency by the ALMA spectral index (epoch 2019.29); sources with SMA flux measurements $<7\sigma$ are excluded.

Table 3
Properties of Detected CH₃OH Maser Lines^a

Torsional State ν_t	Transition Quantum Numbers	Rest Frequency (GHz)	E_{upper}/k^b (K)	Channel Spacing		SMA (2019 Mar) Integrated Flux (Jy km s ⁻¹)	ALMA (2019 Apr)		Integrated Flux Ratio SMA/ALMA
				SMA (km s ⁻¹)	ALMA (km s ⁻¹)		Integrated Flux (Jy km s ⁻¹)	T_b^c (K)	
1	13 ₋₂ -14 ₋₃ E2	199.574851(18)	575.2	0.21	0.12	980	314.0	3.17E+6	3.12
1	18 ₃ -19 ₄ E1	200.887863(31)	812.5	0.21	0.12	137	40.5	1.67E+6	3.38
1	16 ₋₁ -17 ₋₂ E2	201.728147(29)	728.2	0.21	0.21	250	44.9	1.18E+6	5.56
0	12 ₅ -13 ₄ E1	206.001302(15)	317.1	0.21	...	5.0
1	6 ₁ -7 ₂ A ⁺	215.302206(19)	373.8	0.21	...	94.3
1	6 ₁ -7 ₂ A ⁻	217.299205(17)	373.9	0.21	...	246
0	15 ₄ -16 ₃ E1	229.589056(12)	374.4	...	0.12	...	8.6	4.82E+3	...
2 ^d	11 ₃ -12 ₄ A ⁻	330.172526(22)	810.7	0.21	0.12	118	16.4	1.39E+4	7.20
2 ^d	11 ₃ -12 ₄ A ⁺	330.172553(22)	810.7	0.21	0.12
1	15 ₋₅ -16 ₋₆ E2	331.755099(32)	823.9	0.21	0.12	147	37.2	1.22E+5	3.95
1	13 ₋₁ -14 ₋₂ E2	343.599019(26)	624.0	0.21	0.12	738	204.7	1.35E+6	3.61
1	10 ₋₂ -11 ₋₃ E2	344.312267(17)	491.9	0.21	0.12	559	187.0	9.27E+4	2.99
1	15 ₃ -16 ₄ E1	350.286493(25)	694.8	0.21	...	174
1 ^d	18 ₄ -19 ₅ A ⁻	358.354940(27)	877.2	0.21	...	68.0
1 ^d	18 ₄ -19 ₅ A ⁺	358.355121(27)	877.2	0.21
1	3 ₁ -4 ₂ A ⁻	361.236506(17)	339.2	0.21	...	11.1

Notes.

^a Transition parameters were extracted from the JPL Line Catalog (Pickett et al. 1998) compiled from Xu et al. (2008).

^b Energies are relative to the lowest rotational level (0_0) of $\nu_t = 0$ A-type methanol at 0 K.

^c Peak Rayleigh-Jeans brightness temperature computed from peak intensity and deconvolved size (typically 0.1–0.3 of the beam).

^d Blended.

$T_{\text{bg}} = 159 \pm 3$ K (see the methodology in McGuire et al. 2018). This model also reproduces the emission from other hot core-tracing molecules like glycolaldehyde, ethylene glycol, methyl formate $\nu = 0$ and 1, ethanol, and acetaldehyde (full analysis of the hot core line emission will be provided in a future work). Given the observed MM1 peak brightness temperature $T_b = 53$ K in the 0.89 mm ALMA image, and assuming that the dust continuum is becoming optically thick at 0.89 mm (so that $T_b \approx$ physical temperature when the emission is resolved), this implies that the size of the dust emission region is $\sim 0''.14$ (~ 940 au).

3.2. (Sub)millimeter CH₃OH Masers

The 14 new Class II CH₃OH maser lines first detected in these data are presented in Table 3 and Figures 1(d)–(g). All of the newly discovered masers are located near the peak of MM1, the brightest continuum source (Figure 1(b)). The new maser transitions have $E_{\text{upper}}/k = 317.1$ – 877.2 K; the majority are from rotational levels within the $\nu_t = 1$ torsionally excited state. One maser arises from a $\nu_t = 2$ transition, providing the first observational evidence that Class II maser pumping involves levels in the $\nu_t = 2$ state (Sobolev & Deguchi 1994). The brightest maser lines observed with ALMA have $T_b > 10^6$ K. For the seven maser lines that are in common between the SMA and ALMA, we find that the integrated flux density has dropped by a factor of 3–7 during the intervening month; though the velocity extent of maser emission stayed constant. The $\nu_t = 0$ line at 349.1070 GHz, identified as a maser in S255IR-NIRS3 (Zinchenko et al. 2017), was covered in our SMA tuning but not detected.

Figure 2 shows the spatio-kinematic (combined spatial morphology and kinematics) behavior of the SMA and ALMA CH₃OH maser lines and representative thermal lines from the ALMA data. For each plotted line, a two-dimensional Gaussian was fitted to each channel with emission. Channels with signal-

to-noise (S/N) < 12 and < 16 for ALMA and SMA, respectively, are omitted to ensure relative position uncertainties better than 20 mas. In both epochs, the (sub)millimeter CH₃OH masers consistently trace a roughly elliptical curvilinear pattern centered on the continuum peak, with major and minor axes of $0''.20$ and $0''.17$ (≈ 1 light-week), and position angle $+119^\circ$. The brightest masers are located across from each other, to the northeast (blueshifted) and southwest (redshifted). An additional set of spots extending northeast of the continuum peak appears only in the first epoch, only in the highest excitation lines, and primarily at the central ν_{LSR} (Figures 2(a) and (b)). In contrast, the thermal hot core-tracing lines reveal a different morphology, tracing a linear pattern $0''.15$ (~ 1000 au) in length that crosses the continuum peak. Interestingly, for CH₃CN $J = 11$ – 10 , the position angle of this feature changes from $\sim -33^\circ$ in the lowest (coldest) $K = 2$ transition to $\sim -5^\circ$ in the highest (hottest) $K = 6$ transition. This progression could result from a temperature and/or opacity effect, coupled with the emitting region’s geometry.

3.3. G358.93–0.03 Luminosity

Assuming a distance of 6.75 kpc (Section 3.1), along with photometry extracted from 1.1 mm BGPS (Rosolowsky et al. 2010), 0.87 mm ATLASGAL (Schuller et al. 2009), and 70–500 μm Herschel HiGAL (Molinari et al. 2016) survey images for the integrated emission from the G358.93–0.03 region, a single temperature graybody fit yields $T_{\text{dust}} = 28.5 \pm 1.5$ K, implying an $L_{\text{FIR}} \approx 7660 L_\odot$, following the procedure of Towner et al. (2019). We also fit the full SED, including the MIPS GAL 24 μm detection (Gutermuth & Heyer 2015), to the model grid of young stellar objects of Robitaille (2017), using the method described in Towner et al. (2019). The best fits yield L_{bol} of $\approx 20,000 L_\odot$, but because the shorter wavelength data may be contaminated with foreground emission, this value should be considered an upper limit.

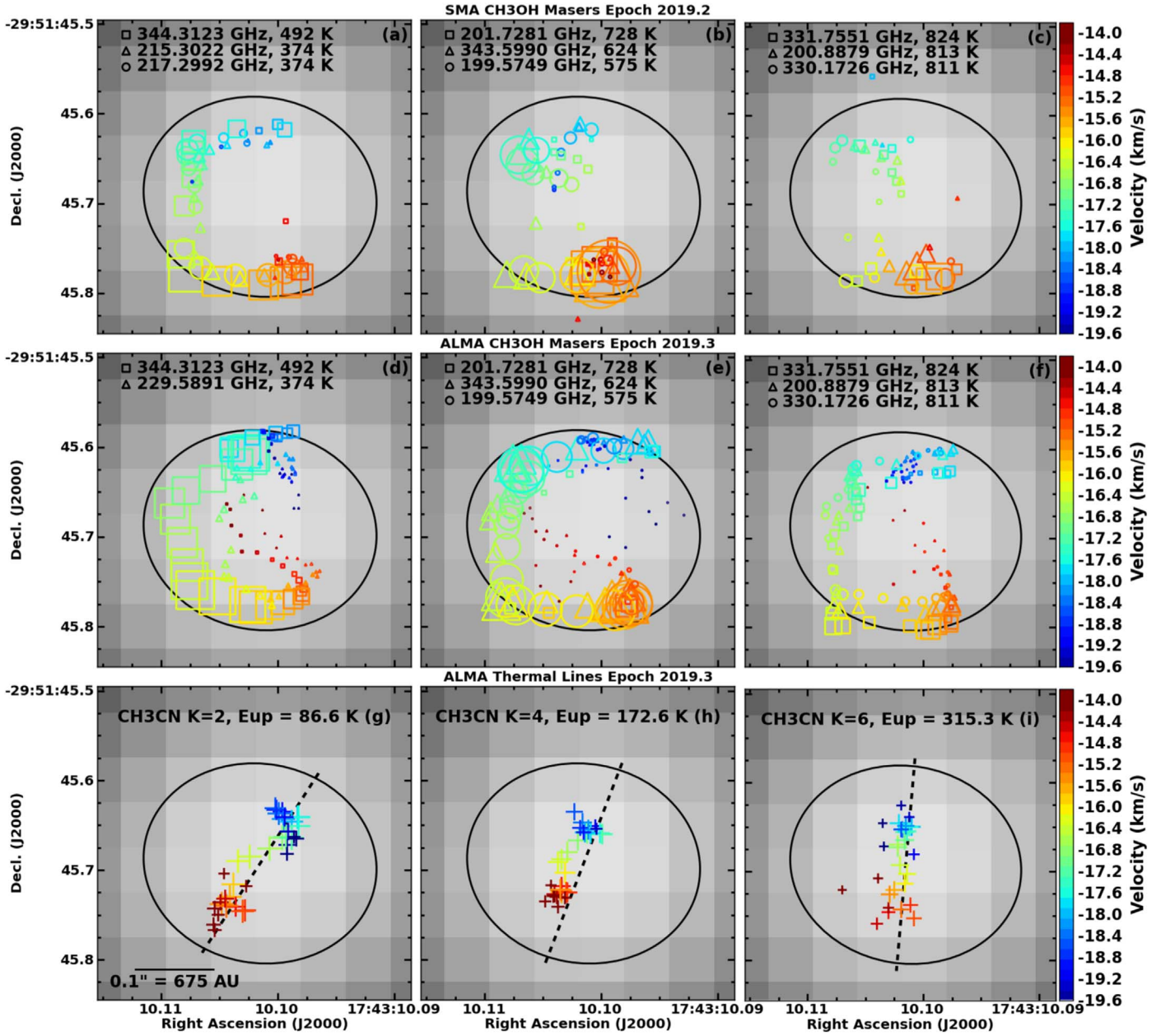


Figure 2. In each panel, the spatio-kinematics of the indicated line(s) is (are) shown on the 0.89 mm continuum image from Figure 1(a) (pixel size 50 mas), zoomed in toward MM1. Each plotted symbol shows the location of the peak emission from a 2D Gaussian fit in each channel ($\leq 0.21 \text{ km s}^{-1}$ wide; the symbols are color-coded by velocity). The fitted relative position uncertainty is 20 mas, while the absolute uncertainty is twice that. Each panel also shows an ellipse representing the deconvolved size (FWHM) of the millimeter continuum emission from MM1 (Table 2). Panels (a–c) show CH_3OH maser lines from SMA, panels (d–f) show CH_3OH maser lines from ALMA, and panels (g–i) show thermal $\text{CH}_3\text{CN } J = 11-10$ lines from ALMA. Symbol size is proportional to intensity on the same relative scale within each row; for SMA the maser symbol size is one-third the ALMA maser symbol size. Panels (g–i) also show position angle vectors (dashed) of -33° , -21° , and -5° , respectively.

Accounting for the distance uncertainty, the plausible luminosity range (for the near distance) is $5700\text{--}22,000 L_\odot$. We measured an 0.87 mm ATLASGAL flux density of $1.10 \pm 0.16 \text{ Jy}$, after making a correction for an estimated 17% line contamination based on the integrated (non-maser) line emission in the ALMA Band 7 data. With this flux density and the T_{dust} estimate, we find a total gas mass of $167 \pm 12 M_\odot$ for the G358.93–0.03 protocluster (assuming a grain opacity spectral index $\beta = 1.7$ and dust-to-gas ratio of 100).

4. Discussion

Maser emission will arise from locations where the physical conditions are favorable for the maser pumping mechanism, and the line of sight affords a velocity-coherent high column density path length. The rapid evolution of the maser flare in G358.93–0.03, with dramatic changes over the course of only 1 month, together with the large spatial scale over which changes have occurred ($\sim 1200 \text{ au}$), require that the impetus for change must be radiative: the timescale for physical movement or bulk changes in the line-of-sight path is far too long. For example, at 6.75 kpc a parcel of gas moving at 100

km s^{-1} would take 16 yr to traverse 50 mas (~ 340 au, 1 pixel of Figure 2).

One explanation for the maser flare is an abrupt change to more favorable physical conditions, such as the rapid heating of dust and gas that occurs in a protostellar accretion event (Johnstone et al. 2013). Comparing our measurement of the 0.87 mm ATLASGAL flux density (1.11 Jy) with the total ALMA 0.89 mm measurement after scaling to 0.87 mm, 1.22 ± 0.04 Jy (using the flux-weighted mean dust spectral index of +3.3), yields a post-flare excess of 0.11 ± 0.19 Jy at 0.87 mm, which is consistent with no change. Previous estimates of the ATLASGAL flux density for this source range from 1.09 to 1.4 Jy (Contreras et al. 2013; Csengeri et al. 2014), with the former being the result of applying a spatial filtering technique, but neither correcting for line contamination. It is surprising that the spatially filtered flux density is reduced from the unfiltered values by 22%–30% given that this source is unresolved by ATLASGAL (the fitted size is smaller than the ATLASGAL beam). Nevertheless, using the spatially filtered value as a lower limit to the pre-flare flux density, and correcting for line contamination (Section 3.1), yields 0.90 ± 0.16 Jy, suggesting a maximum possible excess of 0.32 ± 0.15 Jy. However, this 2σ result is larger than the current total flux density of MM1 scaled to 0.87 mm (0.30 ± 0.01 Jy), suggesting any change was considerably smaller.

It is also feasible that a modest brightening of MM1, which currently represents 25% of the total ALMA flux, is being masked by a commensurate loss in the total flux of the protocluster due to spatial filtering of larger-scale emission by ALMA compared to ATLASGAL’s $19''/2$ beam. Unfortunately, the lack of prior higher-resolution millimeter data prevents us from testing this possibility. The two post-flare (sub)millimeter observations do not show evidence for any significant ($>10\%$) change in the continuum flux of MM1 between the 2019.2 and 2019.3 epochs (Table 2). In summary, the uncertainty in the pre- and post-flare flux densities (and spatial filtering) allow for a modest brightening to have occurred, but it remained steady between 2 and 3 months after the maser flare began, in contrast to the masers. Alternatively, because the heating and cooling timescale of the dust is shorter than the gas (Johnstone et al. 2013), it is possible that modest dust heating was associated with the maser flare, but had already subsided before our SMA and ALMA observations. In contrast, the (sub)millimeter emission of S255IR-NIRS3 increased by a factor of 2 and subsided after 2 yr, while NGC 6334I increased by a factor of 4 and has yet to subside after 4 yr (T. R. Hunter et al. 2017, 2019, in preparation; Liu et al. 2019).

The spatio-kinematic pattern of a partial elliptical ring formed by the CH_3OH masers, especially in epoch 2019.3 (Figures 2(d)–(f)), suggests a coherent physical structure that has been illuminated by a radiative event from the protostar. The pattern is not consistent with simple rotation of an inclined circular disk—in that case the most redshifted and blueshifted emission should be observed at the intersection of the ellipse with its major axis. The distribution of maser spots in G358.93–0.03 is similar to ring-like structures in the 6.7 GHz maser line originally found by Bartkiewicz et al. (2005) toward the massive protostar G23.657–0.127, for which recent proper motion measurements suggest slow expansion rather than disk

rotation (Bartkiewicz et al. 2018). Such a morphology could arise from the walls of an outflow cavity.

Interpreting the velocity gradient in the thermal CH_3CN emission as arising from disk rotation, as seen in other massive protostars (e.g., Ilee et al. 2018), also presents concerns. While the radius and line width would imply a dynamical mass of $(5/\sin i)M_\odot$, the higher-velocity channels do not peak closer to the center of the distribution but instead near the edges, which suggests a ring morphology with edge-on inclination ($i \sim 90^\circ$) for the thermal gas; or simply two sources at different v_{lsr} . Interestingly, the faint redshifted spots in the ALMA maser spot diagrams (Figures 2(d)–(f)) appear to connect with the redshifted side of the thermal gas velocity gradient.

One explanation for the apparent connection of the redshifted maser and thermal gas is a spiral filament of infalling gas, a concept invoked to explain the kinematic structures in thermal species (including CH_3OH) toward G10.6–0.04 (Liu 2017), and in the methanol masers surrounding Cepheus A HW2 (Sanna et al. 2017). Similarly, hydrodynamic simulations predict spiral shapes in fragmenting accretion disks around massive protostars, leading to large accretion outbursts as fragments reach the protostar, a mechanism proposed to explain the outburst in S255IR-NIRS3 (Meyer et al. 2018). Spiral arm structures can also be driven by an encounter between a protostellar disk and a massive companion (Clarke & Pringle 1993; Cuello et al. 2019), including cases that generate a single tidal arm.

In conclusion, while it is clear that a significant radiative event must have occurred in G358.93–0.03 to produce a strong but rapidly declining CH_3OH maser flare with a coherent velocity pattern, coupled with the discovery of numerous new CH_3OH maser lines, the lack of conclusive evidence for dust heating is perplexing. For certain, this event has different characteristics compared to the prior two massive protostellar outburst events (S255IR-NIRS3, NGC 6334I-MM1). Ongoing monitoring of the maser decline (also see MacLeod et al. 2019), future observations of outflow tracers, higher angular resolution dust continuum observations, and detailed investigation of the maser pump conditions will provide essential clues to unravel the nature of this enigmatic maser flare event.











The National Radio Astronomy Observatory is a facility of the National Science Foundation operated under agreement by the Associated Universities, Inc. This paper makes use of the following ALMA data: ADS/JAO.ALMA#2018.A.00031.T. ALMA is a partnership of ESO (representing its member states), NSF (USA) and NINS (Japan), together with NRC (Canada) and NSC and ASIAA (Taiwan) and KASI (Republic of Korea), in cooperation with the Republic of Chile. The Joint ALMA Observatory is operated by ESO, AUI/NRAO, and NAOJ. The SMA is a joint project between the Smithsonian Astrophysical Observatory and the Academia Sinica Institute of Astronomy and Astrophysics and is funded by the Smithsonian Institution and the Academia Sinica. This research used the <https://www.splatalogue.net> spectroscopy database (Remijan 2007).

Facilities: ALMA, SMA.

Software: CASA (McMullin et al. 2007), APLpy (Robitaille & Bressert 2012).

ORCID iDs

C. L. Brogan  <https://orcid.org/0000-0002-6558-7653>

T. R. Hunter  <https://orcid.org/0000-0001-6492-0090>
 A. P. M. Towner  <https://orcid.org/0000-0001-5933-824X>
 B. A. McGuire  <https://orcid.org/0000-0003-1254-4817>
 M. A. Gurwell  <https://orcid.org/0000-0003-0685-3621>
 C. J. Cyganowski  <https://orcid.org/0000-0001-6725-1734>
 R. A. Burns  <https://orcid.org/0000-0003-3302-1935>
 A. Caratti o Garatti  <https://orcid.org/0000-0001-8876-6614>
 J. O. Chibueze  <https://orcid.org/0000-0002-9875-7436>
 T. Hirota  <https://orcid.org/0000-0003-1659-095X>
 K.-T. Kim  <https://orcid.org/0000-0003-2412-7092>
 A. Remijan  <https://orcid.org/0000-0001-9479-9287>
 K. Sugiyama  <https://orcid.org/0000-0002-6033-5000>

References

- Bartkiewicz, A., Sanna, A., Szymczak, M., Moscadelli, L., & van Langevelde, H. 2018, in IAU Symp. 336, *Astrophysical Masers: Unlocking the Mysteries of the Universe*, ed. A. Tarchi, M. J. Reid, & P. Castangia (Cambridge: Cambridge Univ. Press), 211
- Bartkiewicz, A., Szymczak, M., & van Langevelde, H. J. 2005, *A&A*, 442, L61
- Beuther, H., Mottram, J. C., Ahmadi, A., et al. 2018, *A&A*, 617, A100
- Breen, S. L., Sobolev, A. M., Kaczmarek, J. F., et al. 2019, *ApJL*, 876, L25
- Brogan, C. L., Hunter, T. R., Cyganowski, C. J., et al. 2016, *ApJ*, 832, 187
- Brogan, C. L., Hunter, T. R., Cyganowski, C. J., et al. 2018, *ApJ*, 866, 87
- Burns, R. A., Bayandina, O., Orosz, G., et al. 2018, arXiv:1812.09454
- Caratti o Garatti, A., Stecklum, B., Garcia Lopez, R., et al. 2017, *NatPh*, 13, 276
- Caswell, J. L., Fuller, G. A., Green, J. A., et al. 2010, *MNRAS*, 404, 1029
- Cesaroni, R., Moscadelli, L., Neri, R., et al. 2018, *A&A*, 612, A103
- Chen, X., Sobolev, A. M., Breen, S. L., et al. 2019, *NatAs*, submitted
- Clarke, C. J., & Pringle, J. E. 1993, *MNRAS*, 261, 190
- Contreras, Y., Schuller, F., Urquhart, J. S., et al. 2013, *A&A*, 549, A45
- Cragg, D. M., Sobolev, A. M., & Godfrey, P. D. 2005, *MNRAS*, 360, 533
- Csengeri, T., Urquhart, J. S., Schuller, F., et al. 2014, *A&A*, 565, A75
- Cuello, N., Dipierro, G., Mentiplay, D., et al. 2019, *MNRAS*, 483, 4114
- Fischer, W. J., Safron, E., & Megeath, S. T. 2019, *ApJ*, 872, 183
- Fujisawa, K., Yonekura, Y., Sugiyama, K., et al. 2015, *ATel*, 8286, 1
- Gutermuth, R. A., & Heyer, M. 2015, *AJ*, 149, 64
- Hunter, T. R., Brogan, C. L., MacLeod, G., et al. 2017, *ApJL*, 837, L29
- Hunter, T. R., Brogan, C. L., MacLeod, G. C., et al. 2018, *ApJ*, 854, 170
- Ilee, J. D., Cyganowski, C. J., Brogan, C. L., et al. 2018, *ApJL*, 869, L24
- Johnstone, D., Hendricks, B., Herczeg, G. J., & Bruderer, S. 2013, *ApJ*, 765, 133
- Liu, H. B. 2017, *A&A*, 597, A70
- Liu, H. B., Chen, H.-R. V., Román-Zúñiga, C. G., et al. 2019, *ApJ*, 871, 185
- Liu, S.-Y., Su, Y.-N., Zinchenko, I., Wang, K.-S., & Wang, Y. 2018, *ApJL*, 863, L12
- MacLeod, G. C., Smits, D. P., Goedhart, S., et al. 2018, *MNRAS*, 478, 1077
- MacLeod, G. C., Sugiyama, K., Hunter, T. R., et al. 2019, *MNRAS*, submitted
- McGuire, B. A., Brogan, C. L., Hunter, T. R., et al. 2018, *ApJL*, 863, L35
- McMullin, J. P., Waters, B., Schiebel, D., Young, W., & Golap, K. 2007, in ASP Conf. Ser. 376, *Astronomical Data Analysis Software and Systems XVI*, ed. R. A. Shaw, F. Hill, & D. J. Bell (San Francisco, CA: ASP), 127
- Meyer, D. M.-A., Haemmerlé, L., & Vorobyov, E. I. 2019a, *MNRAS*, 484, 2482
- Meyer, D. M.-A., Kuiper, R., Kley, W., Johnston, K. G., & Vorobyov, E. 2018, *MNRAS*, 473, 3615
- Meyer, D. M.-A., Vorobyov, E. I., Elbakyan, V. G., et al. 2019b, *MNRAS*, 482, 5459
- Molinari, S., Schisano, E., Elia, D., et al. 2016, *A&A*, 591, A149
- Moscadelli, L., Sanna, A., Goddi, C., et al. 2017, *A&A*, 600, L8
- Pickett, H. M., Poynter, R. L., Cohen, E. A., et al. 1998, *JQSRT*, 60, 883
- Reid, M. J., Menten, K. M., Brunthaler, A., et al. 2014, *ApJ*, 783, 130
- Remijan, A. J., Markwick-Kemper, A. & ALMA Working Group on Spectral Line Frequencies 2007, AAS Meeting, 211, 132.11
- Rickert, M., Yusef-Zadeh, F., & Ott, J. 2019, *MNRAS*, 482, 5349
- Robitaille, T., & Bressert, E. 2012, *APLpy: Astronomical Plotting Library in Python*, *Astrophysics Source Code Library*, ascl:1208.017
- Robitaille, T. P. 2017, *A&A*, 600, A11
- Rosolowsky, E., Dunham, M. K., Ginsburg, A., et al. 2010, *ApJS*, 188, 123
- Sanna, A., Moscadelli, L., Surcis, G., et al. 2017, *A&A*, 603, A94
- Schuller, F., Menten, K. M., Contreras, Y., et al. 2009, *A&A*, 504, 415
- Sobolev, A. M., & Deguchi, S. 1994, *A&A*, 291, 569
- Sugiyama, K., Saito, Y., Yonekura, Y., & Momose, M. 2019, *ATel*, 12446, 1
- Szymczak, M., Olech, M., Wolak, P., Gérard, E., & Bartkiewicz, A. 2018, *A&A*, 617, A80
- Towner, A. P. M., Brogan, C. L., Hunter, T. R., Cyganowski, C. J., & Friesen, R. K. 2019, *ApJ*, 875, 135
- Urquhart, J. S., Moore, T. J. T., Schuller, F., et al. 2013, *MNRAS*, 431, 1752
- Volvach, A. E., Volvach, L. N., & Larionov, M. G. 2019, *AstL*, submitted
- Xu, L.-H., Fisher, J., Lees, R. M., et al. 2008, *JMoSp*, 251, 305
- Zinchenko, I., Liu, S.-Y., Su, Y.-N., & Sobolev, A. M. 2017, *A&A*, 606, L6